AD_____

Award Number: DAMD17-97-1-7166

TITLE: Measurements of X-Ray Capillary Optics for Digital
Mammography

PRINCIPAL INVESTIGATOR: Sushil D. Padiyar

CONTRACTING ORGANIZATION: State University of New York
Albany, New York 12222

REPORT DATE: September 2000

TYPE OF REPORT: Final

PREPARED FOR: U.S. Army Medical Research and Materiel Command
Fort Detrick, Maryland 21702-5012

DISTRIBUTION STATEMENT: Approved for Public Release;
Distribution Unlimited

The views, opinions and/or findings contained in this report are
those of the author(s) and should not be construed as an official
Department of the Army position, policy or decision unless so
designated by other documentation.

20010424 094

REPORT DOCUMENTATION PAGE

Public reporting burden for this collection of information is estimated to average 1 hour per response, including the time for reviewing instructions, searching existing data sources, gathering and maintaining the data needed, and completing and reviewing this collection of information. Send comments regarding this burden estimate or any other aspect of this collection of information, including suggestions for reducing this burden to Washington Headquarters Services, Directorate for Information Operations and Reports, 1215 Jefferson Davis Highway, Suite 1204, Arlington, VA 22202-4302, and to the Office of Management and Budget, Paperwork Reduction Project (0704-0188), Washington, DC 20503

1. AGENCY USE ONLY (Leave blank)	2. REPORT DATE September 2000	3. REPORT TYPE AND DATES COVERED Final (1 Sep 97 - 31 Aug 00)

4. TITLE AND SUBTITLE	5. FUNDING NUMBERS
Measurements of X-Ray Capillary Optics for Digital Mammography	DAMD17-97-1-7166

6. AUTHOR(S)
Sushil D. Padiyar

7. PERFORMING ORGANIZATION NAME(S) AND ADDRESS(ES)	8. PERFORMING ORGANIZATION REPORT NUMBER
State University of New York Albany, New York 12222 E-MAIL: sp 7409@cnsvax.albany.edu	

9. SPONSORING / MONITORING AGENCY NAME(S) AND ADDRESS(ES)	10. SPONSORING / MONITORING AGENCY REPORT NUMBER
U.S. Army Medical Research and Materiel Command Fort Detrick, Maryland 21702-5012	

11. SUPPLEMENTARY NOTES

12a. DISTRIBUTION / AVAILABILITY STATEMENT	12b. DISTRIBUTION CODE
Approved for public release; distribution unlimited	

13. ABSTRACT *(Maximum 200 Words)*

14. SUBJECT TERMS		15. NUMBER OF PAGES 40
Breast Cancer		
		16. PRICE CODE

17. SECURITY CLASSIFICATION OF REPORT Unclassified	18. SECURITY CLASSIFICATION OF THIS PAGE Unclassified	19. SECURITY CLASSIFICATION OF ABSTRACT Unclassified	20. LIMITATION OF ABSTRACT Unlimited

NSN 7540-01-280-5500

Standard Form 298 (Rev. 2-89)
Prescribed by ANSI Std. Z39-18
298-102

Table of Contents

Section I: Introduction

Results of extensive mammography screenings have shown the need for detection of breast cancer at earlier and more curable stages to have any significant impact on the mortality rate. While new imaging technologies for breast cancer diagnosis like magnetic resonance imaging, breast ultrasound and breast specific positron emission tomography are being developed, x-ray imaging continues to function as a convenient and economical choice for early detection.

A mammographic imaging system is characterized by four crucial parameters: contrast, resolution, absorbed dose to the patient and dynamic range[1]. The differences in the linear attenuation coefficient between carcinoma and normal breast parenchyma are marginal and contrast becomes highly important to detect small differences in soft tissue density. Resolution, which is a measure of the smallest lesion that the imaging system can detect, needs to be high to detect the details of microcalcifications. A small absorbed dose to the breast while maintaining a high image quality reduces the risk of radiation-induced carcinogenesis. Dynamic range, which is defined as the ratio of the largest signal at detector saturation to that of the smallest signal detectable above the intrinsic noise level of the detector, needs to be high to incorporate the variation in x-ray transmission over the area of the mammogram.

Purpose

X-ray capillary optics, coupled efficiently to a direct digital x-ray detector, provide the basis for a system[2] with high contrast, resolution and dynamic range coupled with low patient dose. One of the promising and exciting new detectors in consideration is based on a x-ray photoconductor, such as amorphous semiconducting Selenium, combined with an active matrix array to create a wide area flat panel image detector[3],[4]. This particular detector would convert the x-ray image directly into a digital signal for display, processing and storage.

X-ray capillary optics have a small angular acceptance and do not transmit high angle Compton scattered photons, thereby enhancing image contrast. Loss of resolution commonly encountered in conventional magnification mammography (the geometric blur due to the finite source spot size) is prevented by the use of these optics as they guide the photons along individual fibers and prevent overlap of the beam emerging from spatially close areas. Enhanced contrast and higher resolution consequently, require the patient to be subjected to the same quality x-ray beam for a shorter period of time, thus reducing the dose. Finally, such a system is amenable to mating with a digital detector, allowing computer-assisted analysis of images and providing a high dynamic range.

1.1 X-ray capillary optics

X-rays had created their own niche in the medical industry within a decade of their discovery by Wilhemn Roentgen in 1895[5]. The technology of generating and harnessing x-ray beams to tap their potential in fields like material physics, medicine and protein crystallography have drawn the attention of physicists for a long time. The effort has resulted in sources of intense radiation like third generation synchrotrons and devices to control and manipulate x-rays.

While most other optics for x-rays suffer from narrow angular and spectral selectivity, x-ray capillary optics present unique advantages.
Well-engineered optics can collimate, focus and filter x-rays.[6],[7] Focussed optics can magnify images or demagnify images to mate them to a direct x-ray detector.

The phenomenon of total reflection (also being exploited in fiber optical devices, which have revolutionized the field of optoelectronics) forms the working principle of x-ray capillary optics with air and borosilicate glass ($Si_{22}O_{62}B_{10}Na_3Al_3K_1$) forming the two dielectric media.

1.2 Theory

The complex index of refraction (n) for x-rays is expressed as[8]

$$n = 1-\delta-i\beta \quad \text{..} \quad (1)$$

with

$$\delta = \frac{\theta_c^2}{2} \text{ and } \quad \beta = \frac{\lambda\mu}{4\pi} \quad \text{...} \quad (2)$$

where θ_c is the critical glancing angle for total reflection, λ is the wavelength of the incident x-rays and μ is the mass attenuation coefficient of the material and depends on the incident energy. When λ is much shorter than the plasma wavelength, then the electrons can be considered as free electrons and δ is given by

$$\delta = \frac{Nq^2\lambda^2}{2\pi mc^2} \quad \text{...} \quad (3)$$

where N is the number of free electrons per unit volume, q is the electric charge, m is the electronic mass and c is the velocity of light.

The reflection coefficient, which is the ratio of the intensity of reflected radiation (I_r) to the intensity of incident radiation (I_o) is obtained from the Fresnel equations and is expressed as

$$\frac{I_r}{I_0} = \left| \frac{Sin\ \theta - (\varepsilon - 1 + Sin^2\theta)^{\frac{1}{2}}}{Sin\ \theta + (\varepsilon - 1 + Sin^2\theta)^{\frac{1}{2}}} \right| \quad \text{...........................} (4)$$

where θ is the glancing angle of the incident x rays and ε is the complex dielectric constant of the material given by n^2 .

The β/δ dependency of $\frac{I_r}{I_o}$ is shown in *fig 1* as a function of θ/θ_c
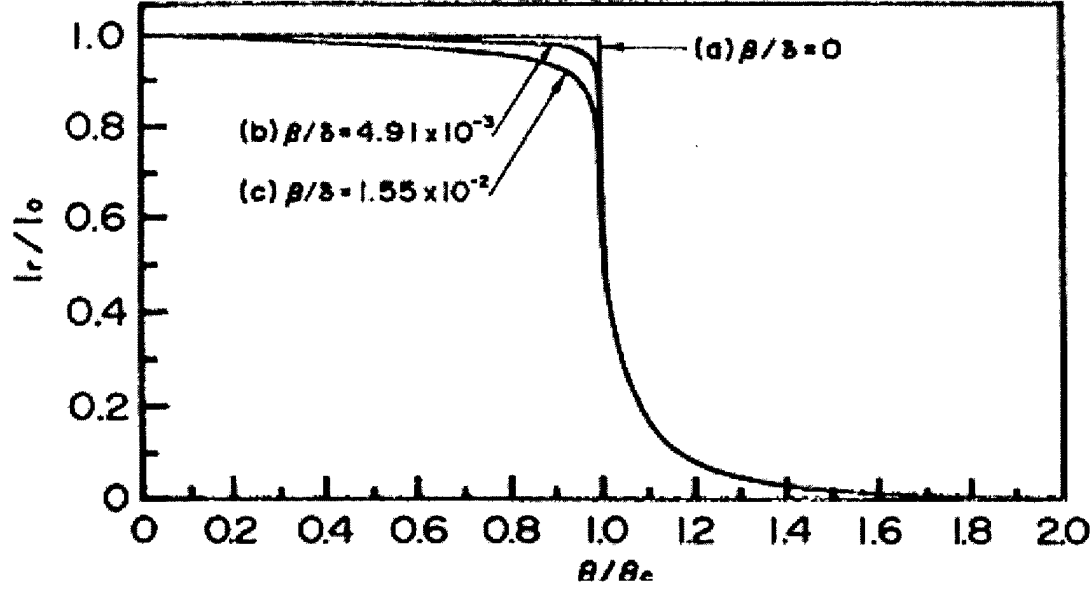
Fig 1 : Theoretical reflection coefficients $\dfrac{I_r}{I_o}$ for the selected $\dfrac{\beta}{\delta}$ as a function of $\dfrac{\theta}{\theta_c}$.

The curve (a) is for $\dfrac{\beta}{\delta}$ = 0 (b) is for $\dfrac{\beta}{\delta}$ = 4.91E-3 at Mo-Kβ and (c) is for $\dfrac{\beta}{\delta}$ = 1.55E-2 at Cu-Kα.

This figure affirms a fast drop in reflectivity at angles greater then the critical angle. It is precisely this property of capillary optics that is beneficial in appropriately designing a scatter rejection device to be employed in imaging systems. Such a scatter rejection optic would enhance contrast, normally diminished due to compton scattered photons reaching the detector plane.

X-ray Capillary optics are made up of many capillary fibers, each fiber being made up of thousands of smooth walled channels, as shown in figure 2.
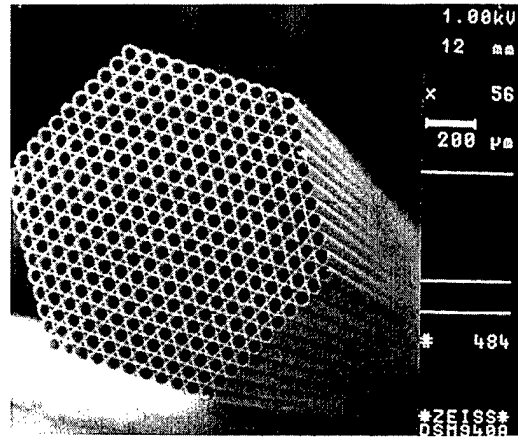
4

Fig 2: A typical micrograph of a polycapillary fiber with channel sizes ~ 50 microns. State of the art manufacturing technology allows adequate control over channel sizes as small as 2 microns.

Section 2: Body of the report

Measurements of Polycapillary X-ray Collimating Optics

Polycapillary x-ray collimating optical lenses can be broadly classified into two categories, a) Monolithic and b) Multi-fiber collimating optics.

2.1 Monolithic optics

Monolithic technology[9] is used for manufacturing optics with small diameters and short focal distances. Monolithic capillary optics are shaped as a single piece so that no external frame assembly is required. A sketch of the profile of a monolithic optic changes along the longitudinal axis as shown in the figure 3.
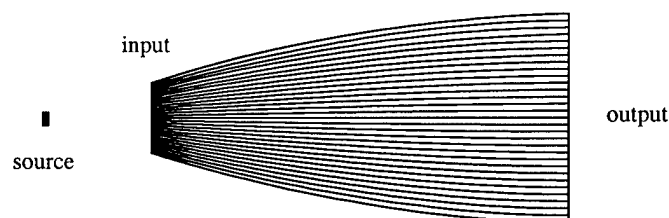

Fig 3: Profile of a monolithic optic. The channels are close-packed. The fiber is shaped as a single monolithic unit.

Since the photons are transported through the fibers by total external reflection, the transmission efficiency is very sensitive to the incident angle. The quick drop

in transmission as the source is moved off axis is shown by the transverse source scan curve in figure 4.
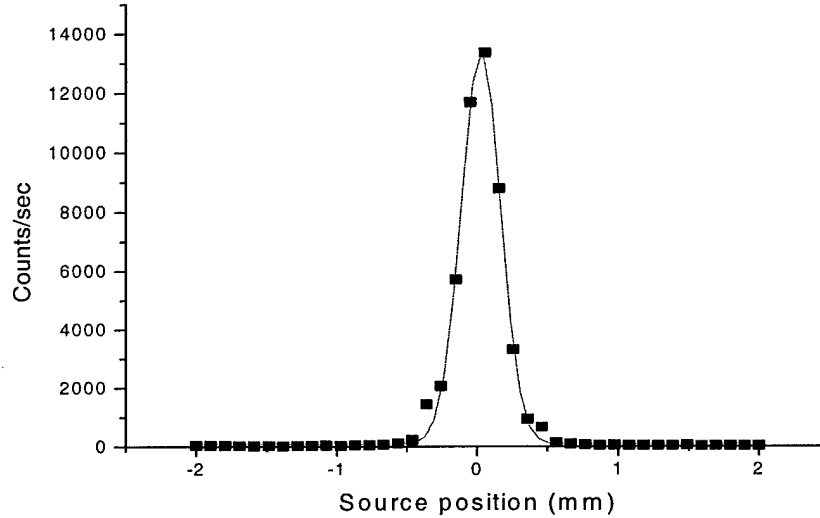

Fig 4: The measured transmitted intensity as a function of source displacement efficiency drops with the source being moved off-axis. The solid line is a gaussian fit of FWHM =0.33 μm.

The rapid drop is due to the increase in the number of reflections required to traverse the length of the fiber as the source is moved off axis as well as the decrease in reflectivity with the increase in the incident angle. A similar effect can be seen as the source is moved along the optic axis in figure 5. Figure 5b shows the x-ray field at the output of the monolithic collimating optic with the x-ray source at the optic focus of 34mm. If the lens is moved closer to the x-ray source, the x rays strike the outer channels at angles greater than the critical angle, and these channels do not transmit, as shown in figure 5a.

(a)   (b)

Fig 5: Polaroid prints of the output from the monolithic optic. The source to lens distances in the two cases are 15 mm (a) and 34 mm (b). A copper target with 16 kV tube voltage was used.

The variation in the transmission of this optic at the Cu Kα line with source-optic distance is plotted in figure 6. An energy window (7.5 keV – 8.5 keV) was chosen

for the measurement. The spatial range over which the transmission of the optic remains as high as 90 % of the maximum value, as the source is moved along the optic axis, is defined as the depth of field, and is 7 mm for the monolithic lens, as seen in figure 6.
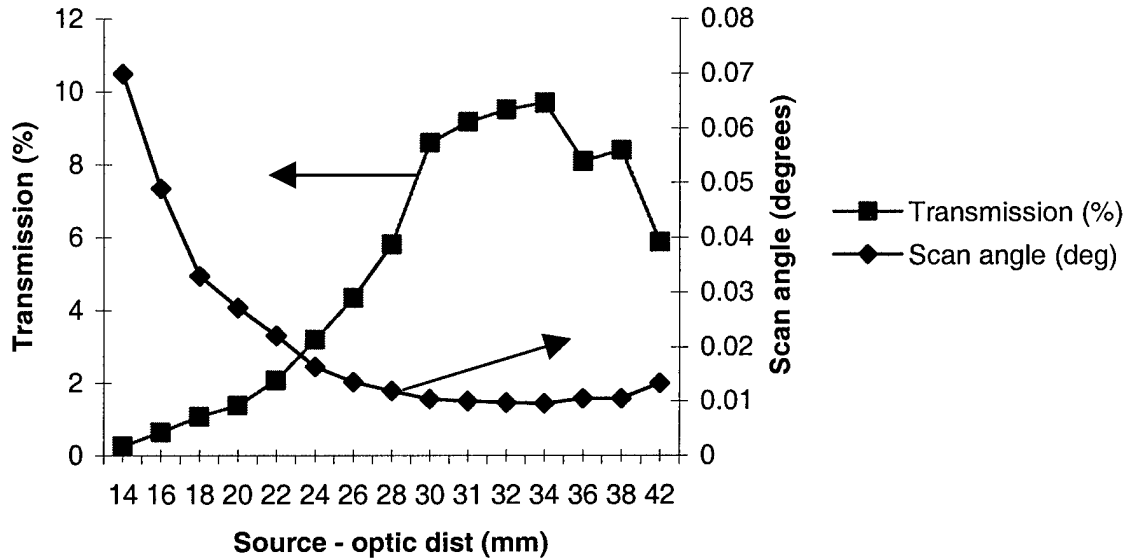

Fig 6: The highest transmission and the smallest scan angle characterize the focal point of an optic.

The focal distance of an optic is the source-optic distance at which the optic transmits the most. Another very reliable method to measure the focal distance of an optic is source scans performed in a direction transverse to the optic axis. The scan angle, defined as the ratio of the width of the scan curve to the source-optic distance, is a minimum at the focal distance, as shown in figure 6. The scan angle curve is more sharply shaped, giving a more accurate determination of the focal distance. A transverse source scan in the focal plane at 34 mm gives a scan angle of 4.8 mrad. The measured scan width at the focal distance is 330 μm. A computation from a Monte Carlo geometrical simulation of an ideal optic gives a width of 280 μm at 8 keV, indicating the presence of small directionality errors in the channels pointing at the input. Transmission performance of this monolithic collimating optic at different photon energies, with the source fixed at the focal point, is shown in figure7. The transmission drops off rapidly with

energy due to the drop in critical angle at higher energies and the sharp bend of the channels necessary to produce the small focal distance.
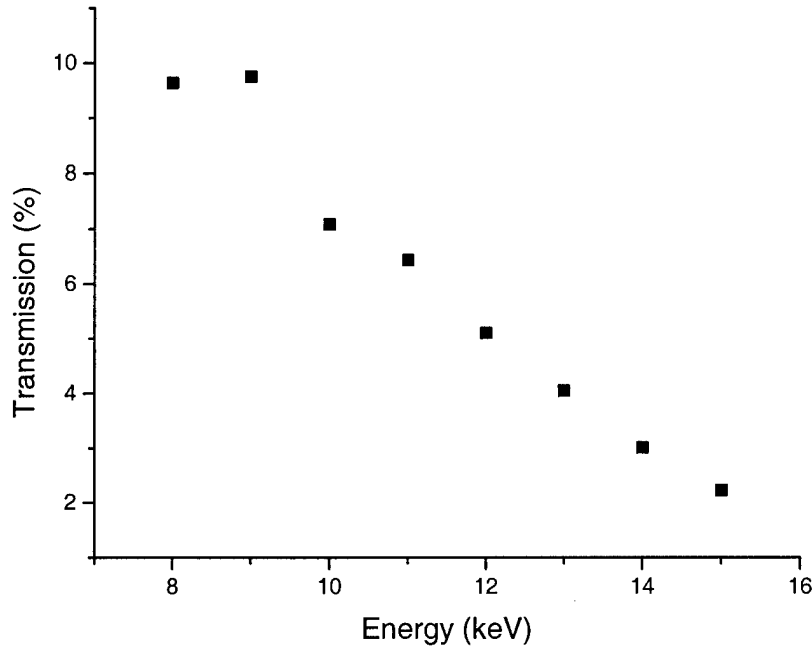

Fig 7: Transmission as a function of energy for the monolithic optic.

2.2 Multi-fiber collimating optics

Multi-fiber collimating X-ray optics are manufactured by meticulously stringing capillary fibers through metal grids and are designed to produce a larger area beam. These optics direct the beam along the capillary channels to produce a quasi-parallel x-ray field. Three prototype multi-fiber collimating optics, the dimensions of which are presented in table I, were measured for this project. The x-ray source used in the measurements listed in tables I and II used a Molybdenum anode with characteristic lines K α and K β at 17.5 keV and 19.6 keV, respectively. A high purity Germanium detector was used to collect the spectra.

Table I.

Optic parameters	Monolithic collimating optic	Multi-fiber collimating optic I	Multi-fiber collimating optic II	Multi-fiber collimating optic III
Input diameter	3.28 mm	23 mm	28 mm	8 mm
Output diameter	3.6 mm	35 mm	30 mm	10 mm
Field shape	Hexagonal	Circular	Square	Square
Channel size	5 μm	17 μm	10 μm	10 μm
Focal distance	34 mm	150 mm	1000 mm	240 mm
Acceptance angle	5.5 deg	9 deg	2 deg	1.8 deg
Transmission (%)	9% at 8 keV	22% at 8 keV 5% at 18 keV	35% at 18 keV	37% at 18 keV

(a)   (b)   (c)   (d)
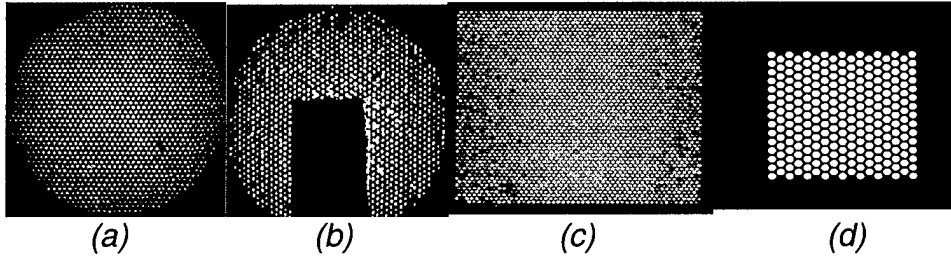
Fig 8: Polaroid images from the three multi-fiber optics described in table I. (a) shows the full multi-fiber I output, (b) the multi-fiber I output with a lead block (c) the output field from the multi-fiber optic II and (d) the uniform output from multi-fiber optic III.

A small rectangular cross-section of the prototype I (17 X 11 mm) was blocked by lead as shown in figure 8b. This part of the optic had been subjected to the white beam at the National Synchrotron Light Source (NSLS) at the Brookhaven National Laboratory (BNL) to study radiation damage effects. The lead block was taken into account while calculating the transmission efficiency of the optic. Source scans carried out in a direction transverse to the optic axis for multi-fiber optic I are shown in figure 9. The minimum scan angle calculated from the width of the scan curves gives a measured focal distance of 150 mm for this optic.
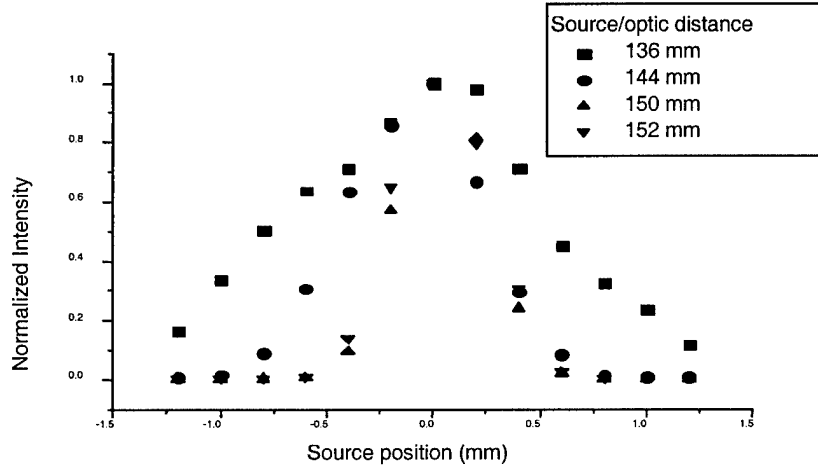
Fig 9: Source scans transverse to the optic axis for prototype collimating optic I at different source optic distances. The source scan is the narrowest at the focal distance, i.e. 150 mm in this case.

The focal distances and the dimensions of these optics enable us to determine the acceptance cone angles of these optics as ~ 9 and 2 degrees for the prototype Collimating Optics I and II respectively.

2.2.1 Transmission

Transmission (T) is defined as the ratio of the flux at the output of the optic to the flux incident on the optic input cross-section. Transmission measurements are performed by collecting the x-ray spectrum through a well aligned optic and then through a small pinhole. (The pinhole is typically smaller than the input diameter of the optic, to avoid dead time losses that can occur due to saturation of the detector). The ratio of the count rate with and without the optic (through the pinhole) gives the transmission. A solid angle correction is applied to this calculation to account for the difference in solid angles subtended by the optic and the pinhole at the source.

$$T = \frac{N_{optic}(E)}{N_{pinhole}(E)} * \frac{\Omega_{pinhole}}{\Omega_{optic}} \quad \dots\dots\dots\dots\dots\dots\dots\dots\dots\dots\dots\dots\dots\dots\dots\dots\dots \quad (5)$$

Where

$N_{optic}(E)$ is the flux at the output of the optic in the relevant energy window.

$N_{pinhole}(E)$ is the flux through a small pinhole in the same energy range.

10

$\Omega_{pinhole}$ is the solid angle subtended by the pinhole at the source and

Ω_{optic} is the solid angle subtended by the optic at the source.

Equation (5) in the case of an optic with a circular cross-section (prototype I) is

expressed as $T = \dfrac{N_{optic}}{N_{pinhole}} \dfrac{(E)}{(E)} * \left(\dfrac{D_{pinhole}}{L_{ps}} * \dfrac{L_{sl}}{D_{optic}} \right)^2$ .... (6)

$D_{pinhole}$, D_{optic}, L_{sl} and L_{ps} being the pinhole diameter, the optic input diameter , the source lens distance and the pinhole-source distance respectively. The results of transmission measurements carried out on the two prototypes are shown in figure 10. The prototype II transmits much better than the earlier prototype in the mammographic energy range, partly due to better alignment of fibers in the grid, but mostly due to the much longer focal length, which allows gentler curvature.
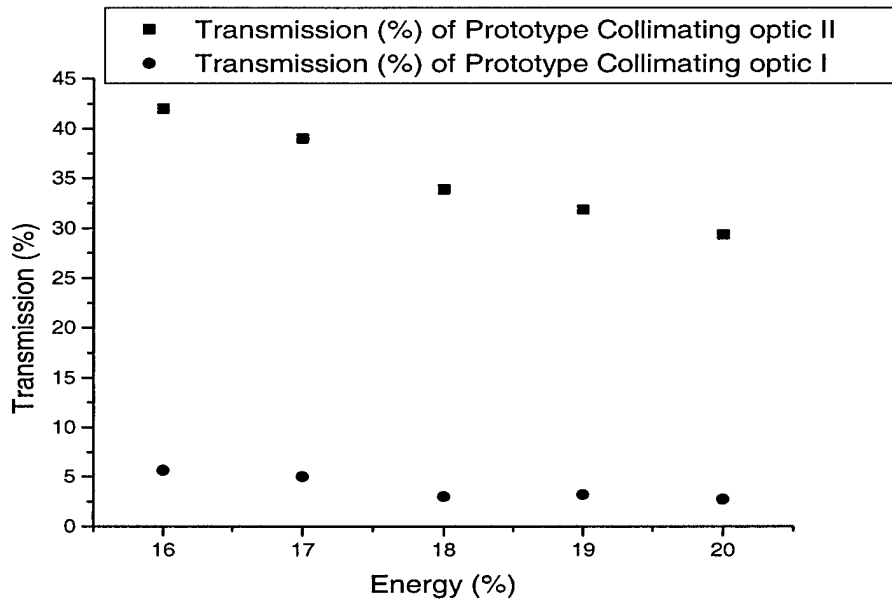

Fig 10: Transmission Vs Energy for prototype collimating optics I & II.

The focal distance is a very important parameter in designing a polycapillary collimator, as a small focal distance ensures a large acceptance angle and thus maximum utilization of the flux emitted by the x-ray source. Multi-fiber optic I with a focal distance of 15 cms has a linear acceptance angle of 9 degrees, while multi-fiber II with a focal distance of 100 cms has an acceptance angle of only 2

degrees. However, multi-fiber optic II transmits significantly higher than multi-fiber I as shown in figure 15, as the fibers in optic II are less bent. The larger focal distance of optic II ensures less bending of the outer channels, which allows transport of high energy photons.

Experimental data gathered from measurements on multi-fiber collimating prototype optics I and II was effectively incorporated in manufacturing multi-fiber optic III, specifically designed for potential applications in digital mammography. Multi-fiber collimating optic III transmits ~ 35% in the 17-20 keV energy range, and provides an uniform output, as seen in figure 8d and figure 11. Future work on this optic involves simulations and accompanying experiments to verify the benefits of collimated beams in mammographic x-ray imaging.
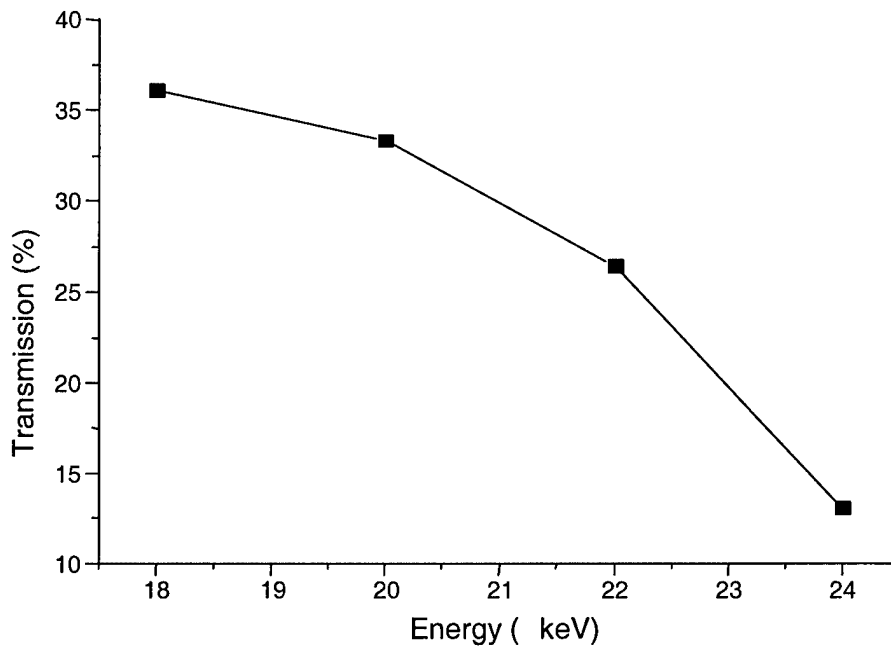
Fig 11: Transmission performance of collimating multi-fiber III. The lens is more specifically designed for mammographic imaging and transmits effectively, in the 17-20 keV energy range.

2.2.2 Divergence

The beam emerging from the optic is quasi-parallel in the sense that the fibers are parallel at the output. This alleviates the problem of penumbral shadowing and also one of unequal magnification of objects at the entry and exit side of the

patient. However, there is local divergence, the divergence of the beam emerging from each individual channel, which depends upon the energy of the radiation. Divergence is a very important parameter because it produces geometric blur in the image and has a profound effect on the system resolution. The local divergence from the individual channels has a value between once and twice the critical angle, for fibers that are well aligned.
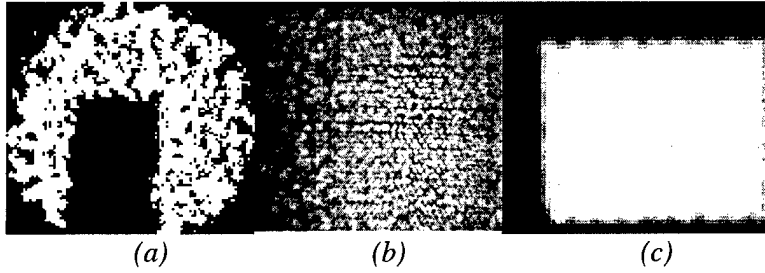

(a)   (b)   (c)

Fig 12: X-ray fields at 30 cms from output of the prototype optics I (a), II (b)and III (c). (The blur is a cause for concern for resolution properties).

This divergence can be seen in comparing figures 8 and 12. In figure 12, which was taken further from the optic, the divergence from the channels has blurred the channel walls. The exit angle divergence of an optic can be determined by Bragg reflecting the output beam off a (100) oriented high quality silicon crystal. Since the crystal diffracts only for a very narrow angular range, rotating the crystal yields the divergence directly, as shown in figure 13.
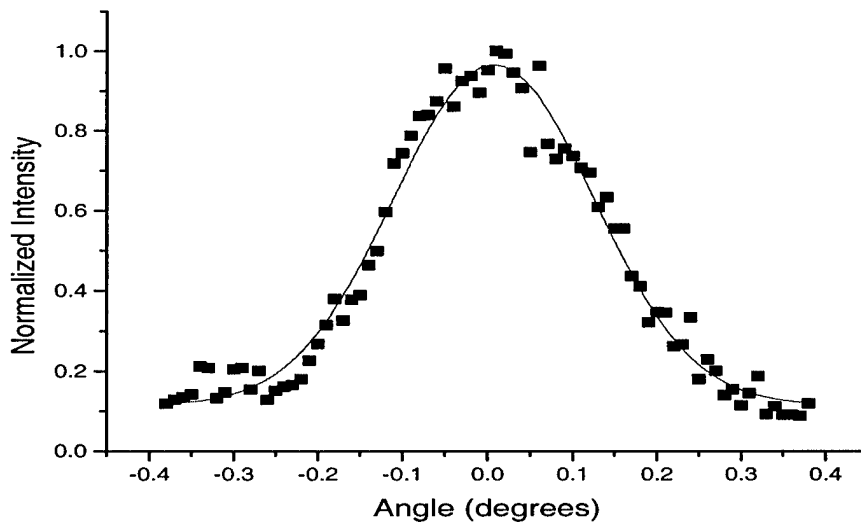

Fig 13: Output divergence measurement of the prototype collimating optic I. Intensity is plotted versus the rotation angle of the crystal.

Section 3: Diffraction Gain

The term defined as "gain"[10] here refers to the increase in the diffracted beam intensity obtained by carrying out an diffraction experiment using a collimating optic in comparison with the same process carried out through a pinhole collimator having the same output divergence as the output divergence of the optic.

The prototype collimator I yields a gain of 18 in comparison with pinhole collimated diffraction.
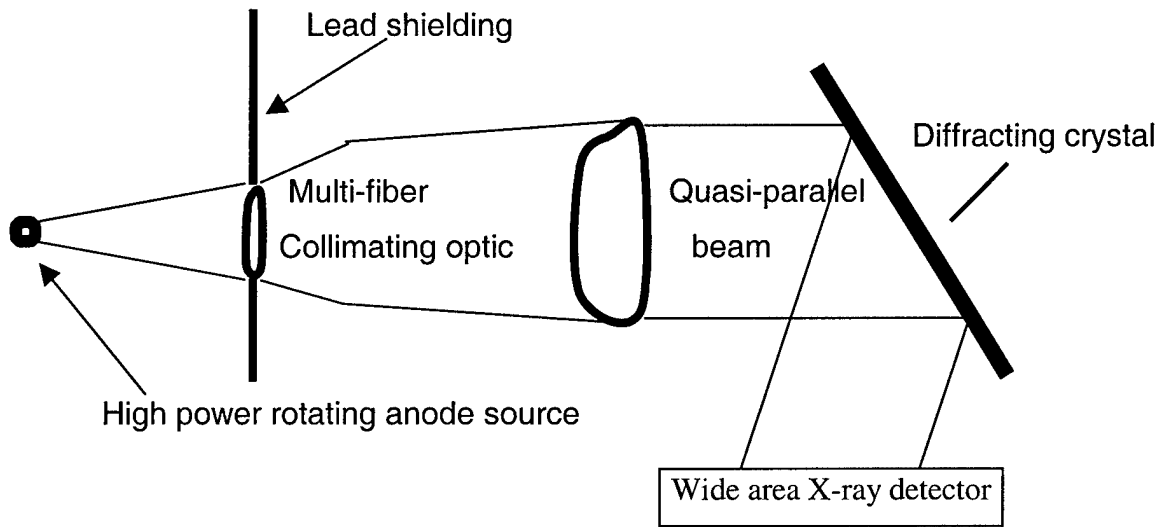

Fig 14: Set-up for monochromatic X-ray imaging experiment. The quasi-parallel output from a multi-fiber X-ray collimating optic is diffracted off a high moscicity crystal to obtain a sufficiently intense and parallel monochromatic beam.

3.1 Monochromatic Imaging

High diffracted beam intensities are desired to produce intense and parallel monochromatic beams[11] as such beams lead to increased resolution and enhanced contrast. The "diffraction gain" described above has interesting connotations as higher diffracted beam intensities can be obtained from an optic with a low output divergence and well aligned fibers.

Contrast between carcinoma and breast parenchyma that is usually diminished due to the small differences in linear attenuation coefficient can be significantly enhanced by the use of monochromatic beams[12],[13]. In addition, the distance between the patient and the source becomes irrelevant due to the parallel nature

of the diagnostic beam. This parallel beam renders possible an adequately large air gap to avoid Compton scattered photons at the detector plane. The problems inherent in a divergent beam (from a finite source spot) are simply not encountered. Fig 14 demonstrates the schematic for such an experiment.

3.2 A Feasibility Analysis

Presented below is a feasibility analysis for acquiring such monoenergetic beams by using a rotating anode source in conjunction with the prototype collimating optic II, which transmits close to 60 % at the copper characteristic K α line (8.5 keV). While this calculation is based on the Cu characteristic line, because of the availability of a high power Cu source in house, it is relatively straightforward to extrapolate it to energy ranges desired for mammography. The output of the collimating optic that is quasi-parallel and polychromatic can be made parallel and monochromatic by diffracting it off a crystal.

Consider a rotating copper anode operated at 6 kW power (30 kV, 200 ma). The flux from a copper anode, emitted isotropically is expressed as

$$F_{Cu} = 2.3*10^{-5} \frac{photons}{electron} * I * (E - E_0)^{1.63} \dots\dots\dots\dots\dots\dots\dots\dots\dots \quad (7)$$

Where E_0 is the energy of the characteristic line being considered and E is the maximum energy in the beam i.e the kVp and I is the tube current.

The flux after the lens is $F_{lens} = F_{Cu} * \frac{\Omega_{optic}}{\Omega} * T_{optic}$, where Ω_{optic}, Ω and T_{optic} represent the solid angle subtended by the optic entrance at the source, the total solid angle of emission (2π) and the transmission of the optic respectively.

Operating the source at 30 kVp and 200 ma gives an integrated count rate of $1.6 * 10^{11}$ photons/sec after the collimating prototype II.

The reflection efficiency of a diffracting crystal depends upon its angular bandwidth. This calculation is based on a Silicon crystal with a bandwidth of 0.02 mrad. The output divergence of each polycapillary channel is less than twice the critical angle. The output angular divergence from a polycapillary fiber is fit with a gaussian with full width at half maximum (FWHM) of 2.25 mrad. The fraction of photons that would lie within the angular acceptance angle α, of a crystal is given by

$$f(\alpha)=\frac{1}{\sigma\sqrt{\pi}}\int_{-\alpha}^{\alpha} e^{-\left(\frac{\theta}{\sigma}\right)^2} d\theta$$, where $\sigma = \frac{FWHM}{2\sqrt{\ln 2}}$. With α= 0.02 mrad this fraction is

1.4 %.

The percentage of photons reflected by the crystal is obtained by multiplying the angular fraction f(α) by the fraction of photons emitted in the required energy range, n(ΔE) and the efficiency of reflection which is almost unity in this case.

The energy bandwidth for Bragg reflection is $\Delta E = \frac{\Delta\theta}{\theta} * E$ where θ is the Bragg

angle for the (400) reflection from silicon. The energy band width is about 0.3 eV, which is about one twentieth the width of a characteristic emission line from a tube source. For a copper target with tube potential of 30 kV, approximately 20 % of the emission lies in the K α line. This means about 1 % of the emission in the 0.3 eV portion of the bandwidth, n(ΔE) = 0.01.

The integrated count rate after the crystal is then

$F_{crystal} = F_{lens}$ * f(α)* n(ΔE)

or $F_{crystal}$ = 2.25*10^7 photons / sec.

The flux obtained could be increased by increasing the tube loading and also by increasing the angular acceptance of the crystal. Highly mosaic crystals are considered good candidates for monochromator design due to their higher integrated reflectivities[14]. Highly oriented pyrolytic graphite, for instance, has a bandwidth of 5 mrad. By reflecting photons incident over this larger angular range would yield a higher reflected beam intensity). An angular bandwidth of

0.5 mrad for instance would give f(α) = 39 % and this would give a reflected

beam count rate of $\quad 3.1 * 10^9 \dfrac{photons}{\sec}$.

The calculation demonstrates that sufficient monochromatic beam intensity could be obtained from a combination of rotating anode sources, which can typically operate above 18 kW power and high mosaicity crystals.

Section 4 : Uniformity Scan of output cross-section of prototype optic I

A 650 μm pinhole was scanned two-dimensionally across the output of the optic with scan step sizes of 750 μm. Fig 15 shows the results of this uniformity scan, which is consistent with the image in figure 8. The position of the lead block is clearly visible and blocks off a significant portion of the centrally located straight fibers that usually transmit very well. The prototype I largely presents a non-uniform output intensity profile. This optic was designed for 8 keV radiation and is too highly curved to work well at 20 keV. The prototype collimating type II transmits much higher in the energy range of interest for mammography and also has demonstrated a superior output uniformity as seen in figure 16.
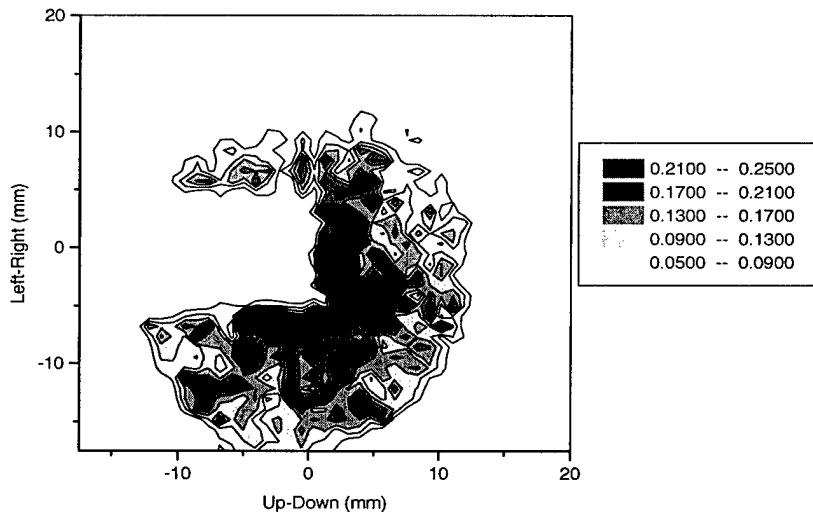

Fig 15: Output Intensity distribution from the prototype collimating optic I in the mammographic energy range 17-20 keV.

20 keV   30 keV

0.4375 -- 0.5000

0.3750 -- 0.4375

0.3125 -- 0.3750

0.2500 -- 0.3125

0.1875 -- 0.2500

0.1250 -- 0.1875

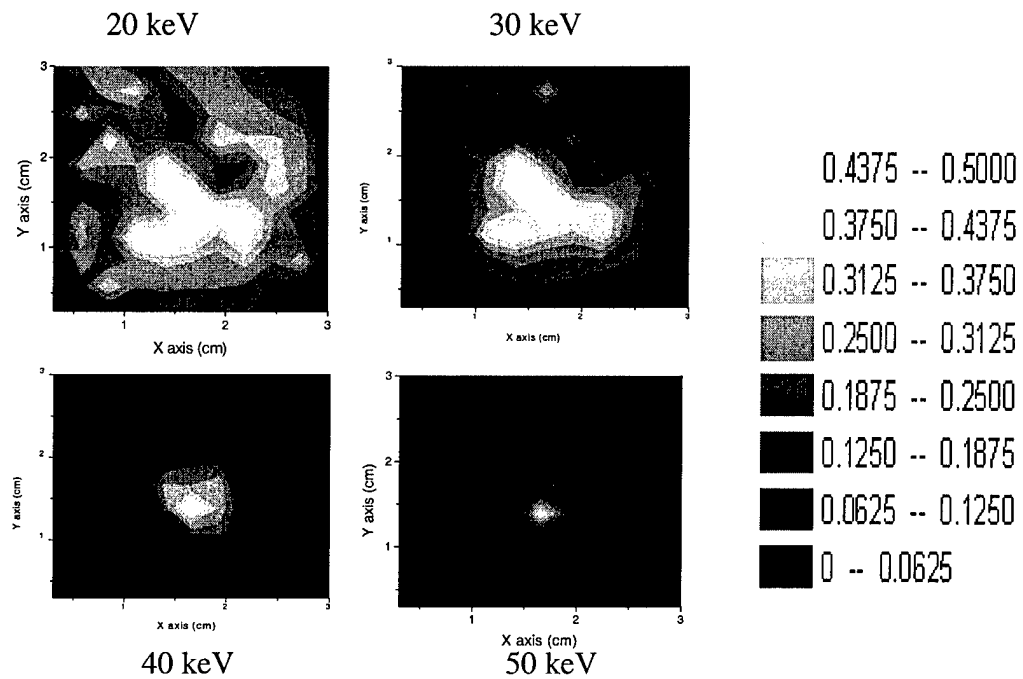0.0625 -- 0.1250

0 -- 0.0625

40 keV   50 keV

Fig 16 : Output normalized intensity distributions for multi-fiber optic II for different x-ray energies. The measurements are at 20, 30, 40 and 50 keV respectively, and demonstrate good uniformity upto 30 keV.

Section 5 : Linear Tapered Magnifying Scatter-Rejection Optics

Four linearly tapered optics were measured for performance characterization in connection to work in magnification, scatter rejection and contrast. These optics, unlike the collimating optics of section II would be used as post-patient "grids". Table II gives the dimensions and the performances of two of these optics.

Table II.

| Prototype Taper I	Prototype taper II
Profile : Linear	Profile : Linear
Input diameter: 2 mm.	Input diameter : 1.9 mm
Output diameter : 4 mm	Output diameter : 3.82 mm
Input channel diameter : 5 μm	Input channel diameter : 4.9 μm
Output channel diameter : 10 μm	Output channel diameter : 9.8 μm
Optic length : 320 mm	Optic length : 350 mm
Transmission efficiency @ Mo K lines = 5 – 7 %.	Transmission efficiency @ Mo K lines: 9 – 12 %.
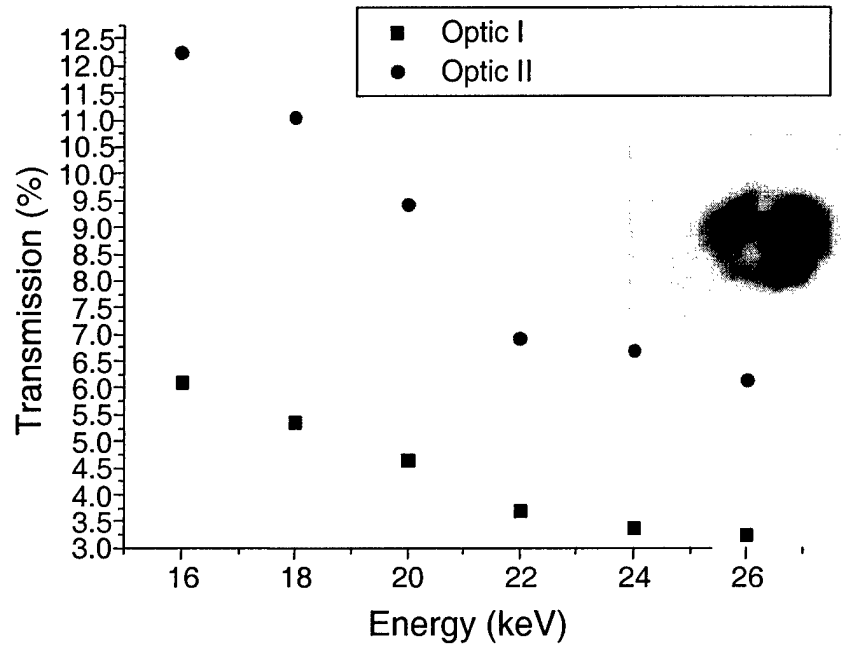
Fig 17: A comparison of transmissions of the two linear tapered prototypes. The figure in the inset shows the output profile of optic I.

Figure 17 compares the transmissions of these two prototypes as a function of energy, whereas the polaroid image in the inset reveals defect structures in output from optic I

5.1 Defect Analysis

An understanding of the poor transmission performance and the nature of the defects in prototype taper I was sought by snapping the optic into parts, here onwards referred to as optic A and optic B respectively. Optic A is the longer piece (22 cm long) and whose output end formed the output end of the original optic. Optic B formed the shorter piece (10 cm long) whose input end formed the input end of the original optic. The transmissions of Optic A and Optic B along with the performance of the original optic, as a function of energy are plotted in figure 18.
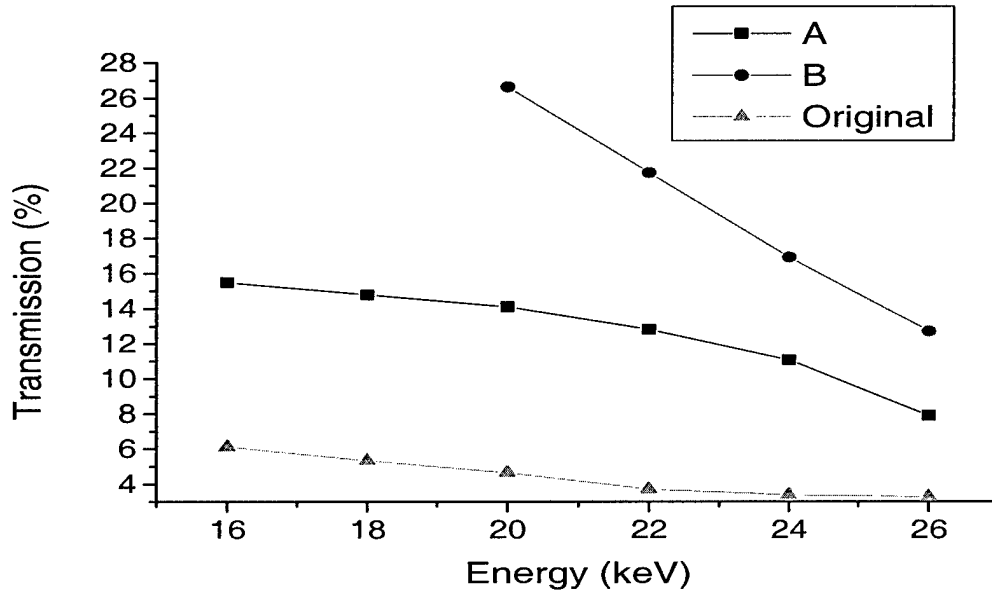
Fig 18: Individual transmissions of the two pieces A and B that made up linear prototype I, in comparison to the transmission of the whole optic.
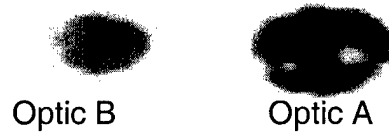

Optic B   Optic A

Fig 19: Output images from optic A (22 cm long) and optic B (10 cm long). The defect is seen to be localized to optic A.

Both Optic A and optic B transmit much higher than the single optic that they constituted before being snapped. This is easy to understand as the transmission depends on the length of the optic, i.e. T = FR^m, where R is the reflectivity of the channels and depends on the incident angle as shown in fig 1 and m is the number of reflections the individual photons undergo between being incident on the input end and emerging from the output end of the optic. F is the fractional open area, which is the part of the input cross-section that is open, i.e, not blocked by the walls delineating the channels. Figure 19 shows output images, taken by exposing T57 Polaroid film to the beam exiting optic A and optic B respectively. The defects are confined to optic A.
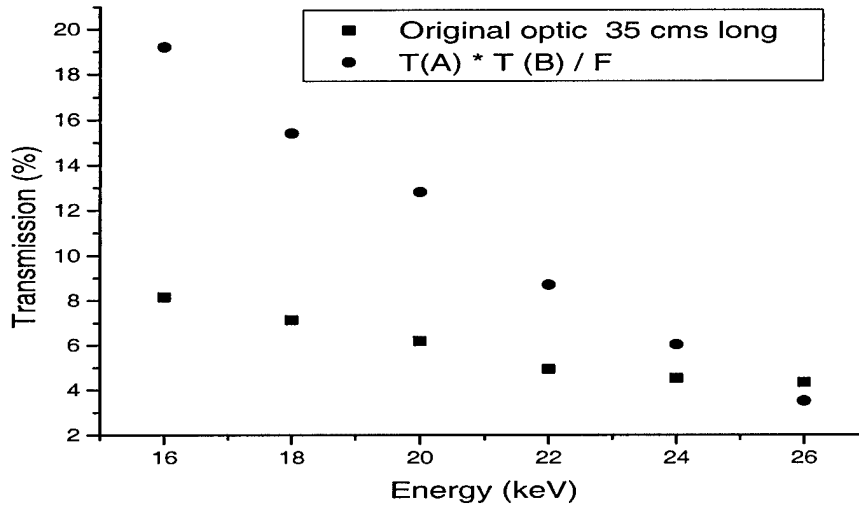
Fig 20: A comparison of the transmission of the original prototype I with the product of the transmissions of optics A and B, where T(A), T(B) and F represent the transmission of optic A, transmission of optic B and the fractional open area of the optic respectively.

Fig 20 illustrates the difference between the transmissions of the unsnapped optic and the product of the transmissions of optic A and optic B divided by the fractional open area of the optic, which was close to 50 % (The transmission of the optic is a product of the fractional open area and the reflectivity of the channels that transport the X-ray photons). This was because the second optic,Optic A now has a source to optic distance longer than that of the original optic. This results in smaller incident angles, thereby increasing the reflectivity. This leads to higher transmission values for optic A by itself than for when it follows optic B. Simulations[15] were tried for straight fibers with channel sizes fiber dimensions matching that of the optic and these generally point to a combination of waviness and bending[16] that causes the transmissions of these optics to drop off rapidly at higher energies. Figure 21 shows the match between experimental results and simulations.

Experimental and simulated transmissions.

- ◆ orig opt 32 cms long
- ■ opt A 22 cms long
- opt B 10 cms long
- + Simulated fiber 32 cms long, B = 220 m, W = .09 mrad.
- ✕ Simulated fiber 22 cms long, B= 120 m, W = .1mrad
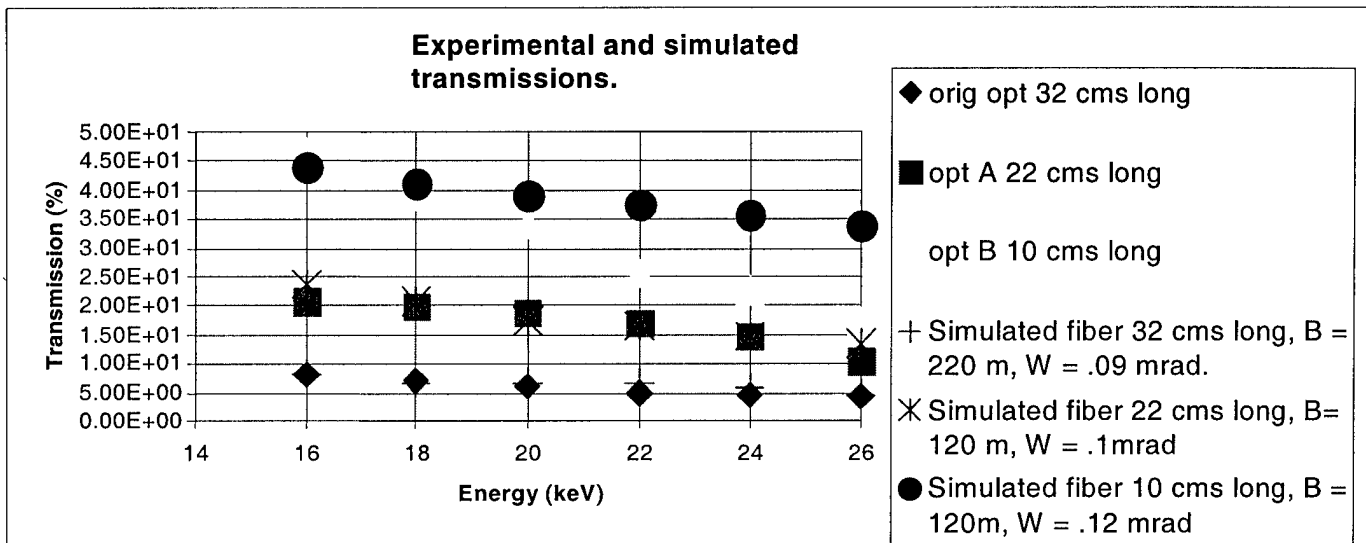- ● Simulated fiber 10 cms long, B = 120m, W = .12 mrad

Fig 21: Simulations carried out on straight fibers yield information on the waviness and bending of the fibers used in the manufacture of this prototype.W is the random tilt angle of the channel walls and B is the radius of curvature of the nominally straight fiber. While a combination of waviness and bending provides information on the transmission performance of the original optic and optic A, the performance of optic B necessitates a simulation code for linear tapered lenses.

Bending has dimensions much larger than the wavelength being used and arises due to profile deformities. Waviness has smaller dimensions and arises due to the local tilting of the channel walls. These simulations assume a straight fiber with no taper. A better understanding of these problems shall be acquired after the Monte Carlo simulation code that is being developed to characterize the performance of linear tapered optics becomes available.
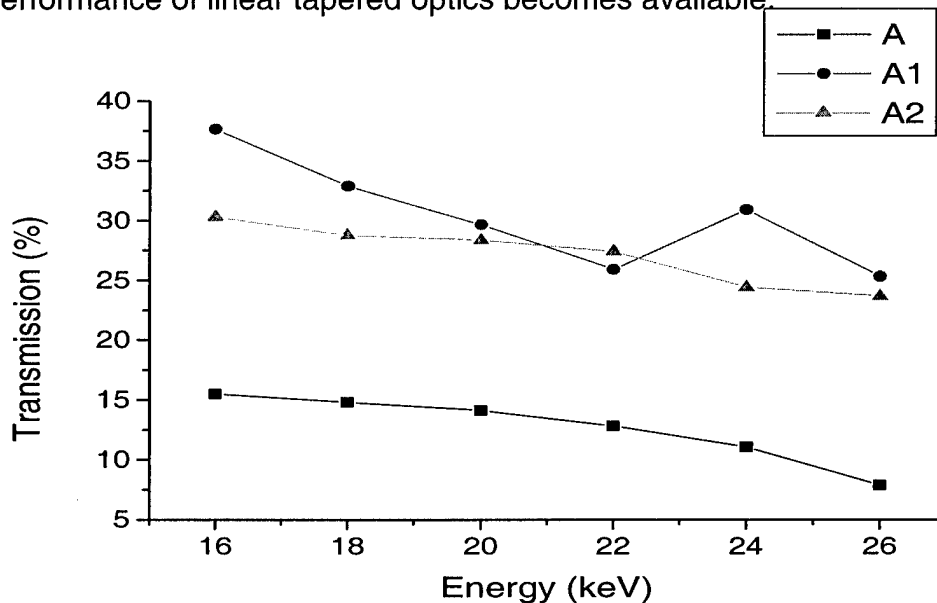
Fig 22: Transmission performances of optic A (22 cms long) in comparison to optic A1 and optic A2 (11 cms long, apiece).

Optic A   Optic A2

Fig 23 : Output images from optic A and optic A2 reveal defects in both pieces.

Since the defects were detected to be confined to Optic A, this piece was consequently snapped into smaller parts and transmission measurements and output x-ray field images were obtained to gather defect information as shown in figure 23. Optic A1 and optic A2 were both 11 cms long and revealed the presence of the defects leading to a non-uniform output intensity profile as seen in figure 23. Optic A2 was divided into A21 and A22, both 5.5 cms long. The defect isolation into optic A21 is seen in the image in figure 24 and the transmission measurements of figure 25.

Optic A2   Optic A21   Optic A22
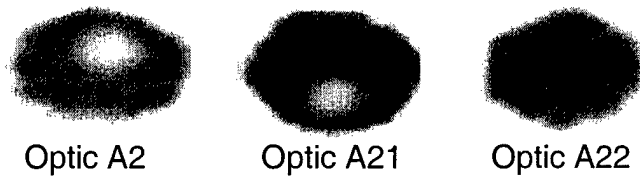
Fig 24 : Optic A2 carrying the defect was further studied by dividing into pieces A21 and A22. The defect was confined to the piece A21, 5.5 cms long.
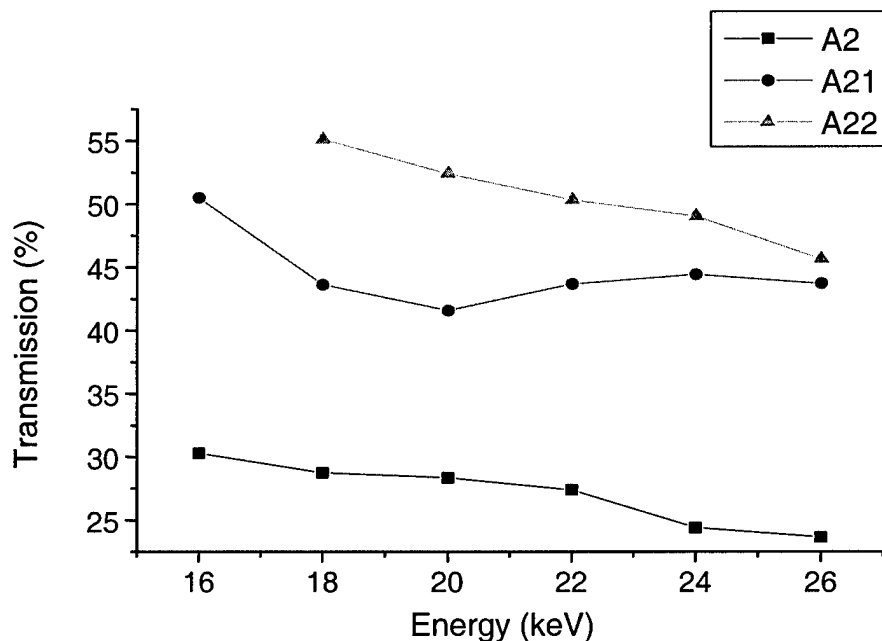
Fig 25:Transmission vs Energy for optic A2 (11 cms long), optic A21 and optic A22 (5.5 cms apiece)

The transmission of the defective piece is higher at 24 keV than at 20 keV, contrary to what is expected from the decrease in the critical angle for total reflection with an increase in the photon energy. The transmission dip cpuld be due to glass blockage in the channels, which would be more transparent at higher energies. These glass blockages concentrated in the defect ridden regions are seen in the images taken under an optical microscope in reflection mode, in figure 26.
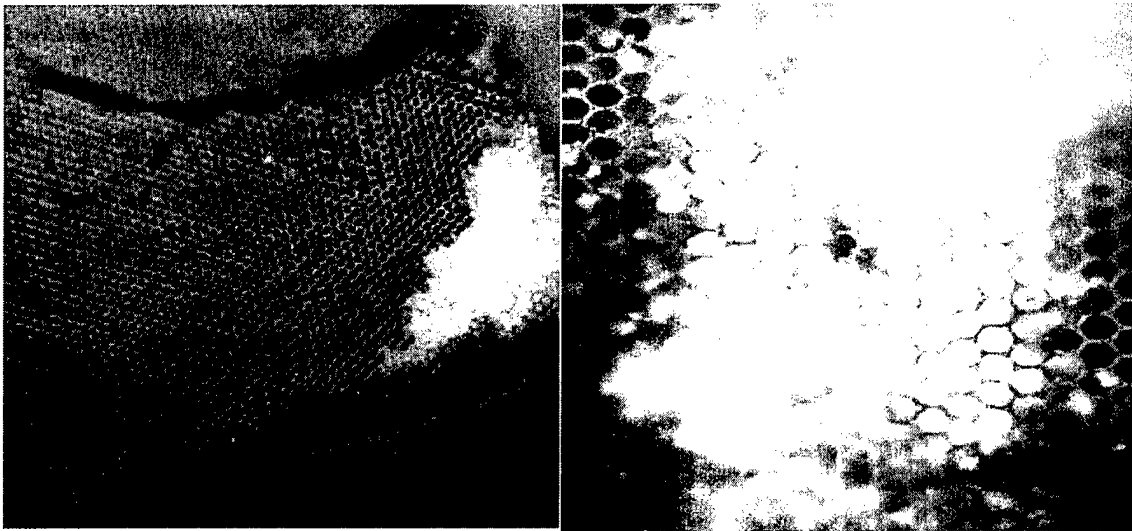

Fig 26 : Optical microscope images for the defective piece A21 demonstrate glass blockages in channels and fused regions.
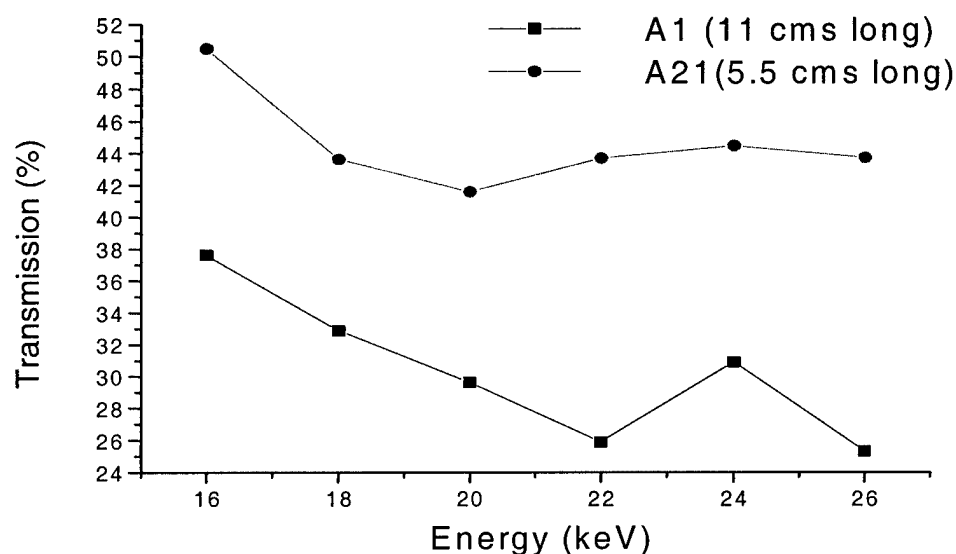
Fig 27 : Defect prone pieces A1 and A21 show a dip in transmission at lower energies. Dense glass blockages could account for this effect.

The dip in transmission at lower energies for optic A2 and A21 due to the glass blockages is seen in figure 27. Absorption at lower energies seems reinforced by the rise in the Brehmsstrahlung spectrum obtained through the optic as shown in figure 28. The direct beam (no optic) spectrum collected for the same time interval through a small pinhole (200 μm) in the same energy range (22-30 keV) is flat.
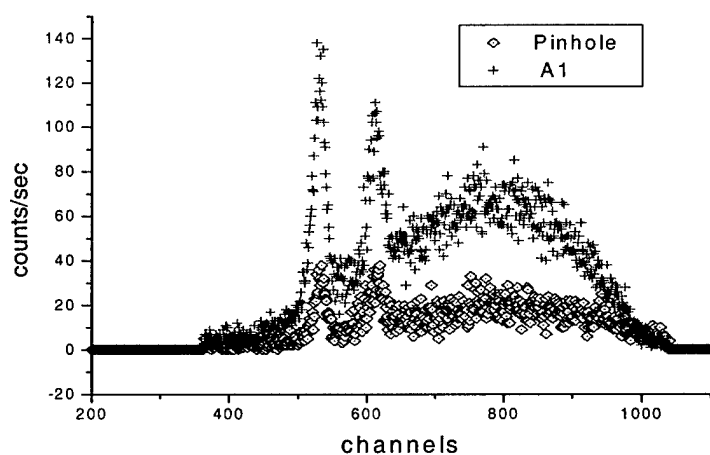

Fig 28 : X-ray spectrum collected from the output of optic A21 and through a small pinhole. The pinhole spectrum is flat in the channel range 600-1000, corresponding to an energy window 22-30 keV.

5.2 Source scans of prototype linear taper II.

Source scans and measurements of lens transmission as the source is moved off axis, are shown in figures 29 and 30, for various source-optic distances and photon energies respectively.
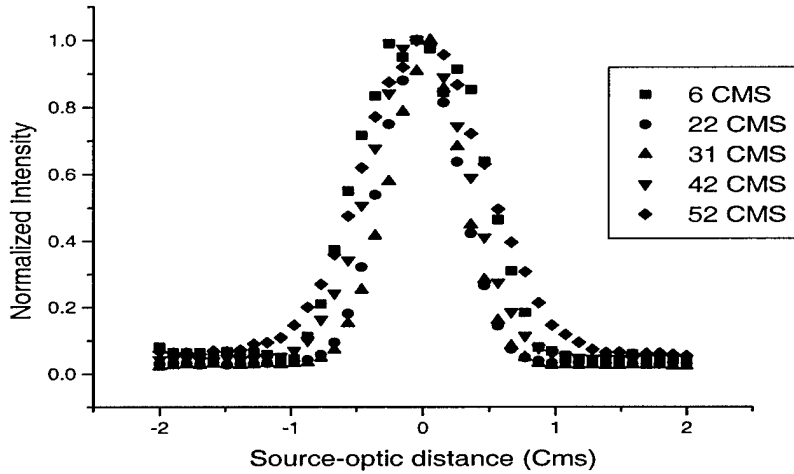

Fig 29 Source scans as a function of the source-lens distance.

Figure 29 determines the focal point of this optic at 31 cms. The source scans are noticeably wider at distances longer or shorter than the focal distance. Both these scans demonstrate the excellent ability of these optics to efficiently reject off-axis radiation, a property highly desired in anti-scatter grids. The narrower scan widths at higher energies seen in figure 31, are due to the smaller critical angle for total reflection at higher energies.
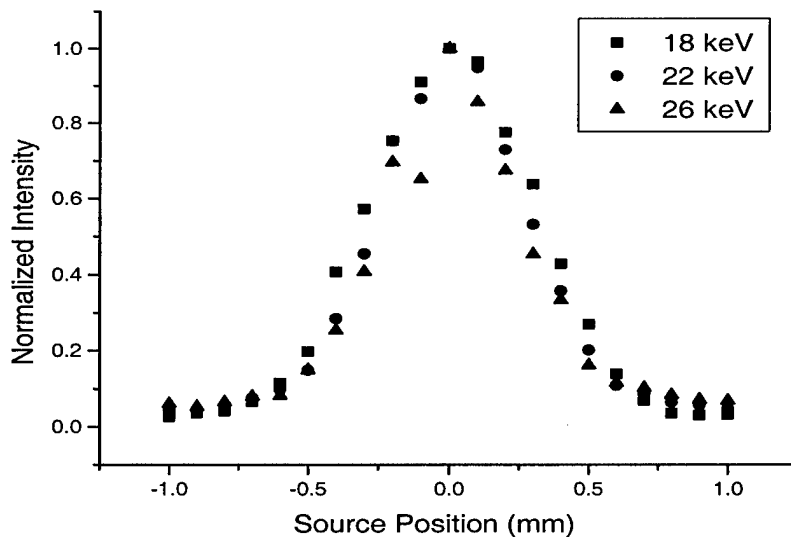

Fig 30 Source scan at the focal plane as a function of energy.

5.3 Transmission Uniformities of Prototype linear taper II.
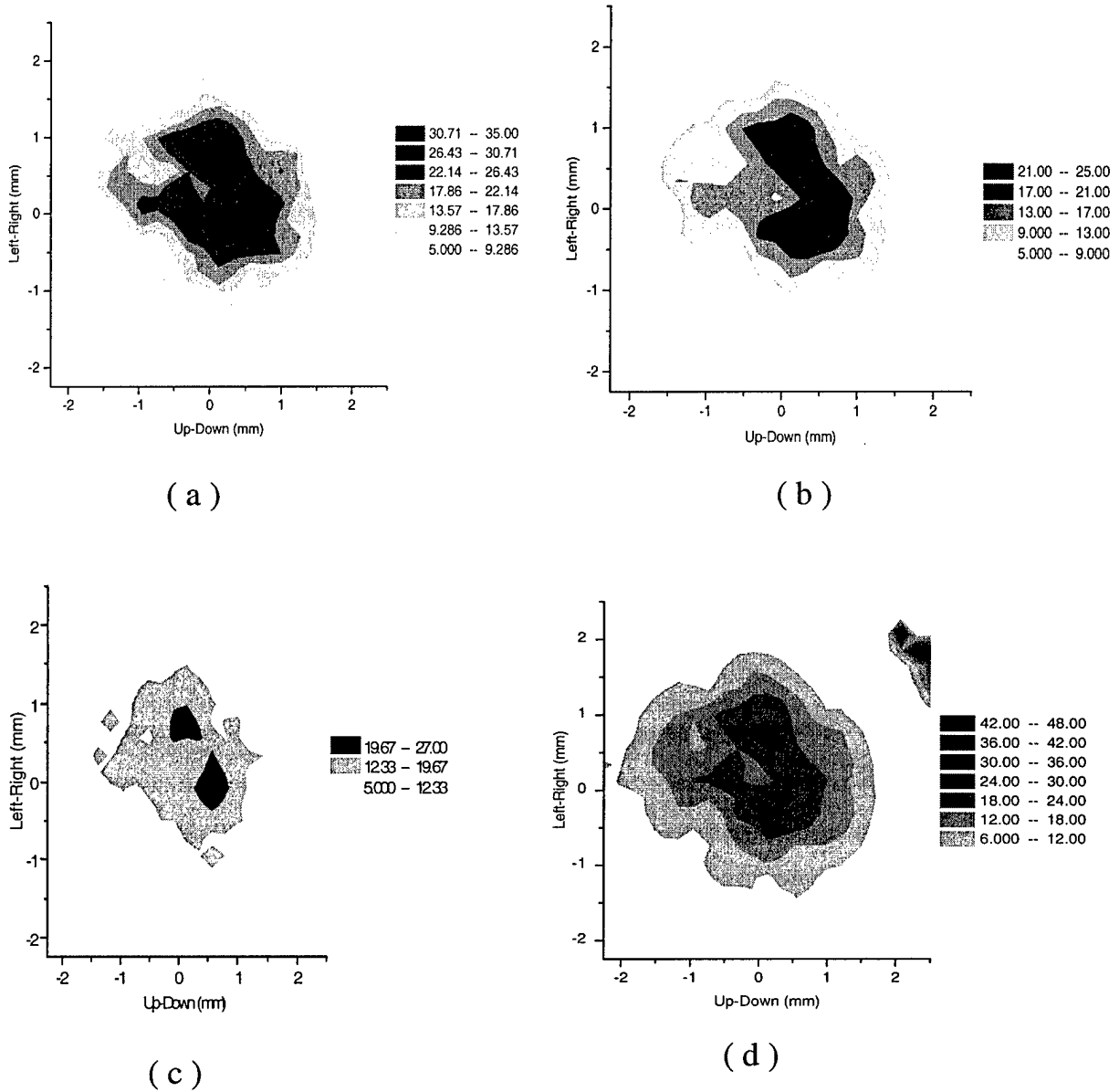

(a)

(b)

(c)

(d)

Fig 31 : Transmission uniformity at 14 keV (a) and 18 keV (b). Transmission uniformity at 22 keV (c) and the whole spectrum (d) (kVp = 26 kV)

Figures 31 a through 31 d are contour maps derived from a uniformity scan carried out at the output of the prototype linear taper II and yield information on the performance of localized regions of the optic. The central core of the optic transmits well essentially due to the straight profile of these fibers, but as we move away from this region, bending and waviness again appear. The cross-

section that transmits is noticeably smaller at higher energies. This is because achieving a good transmission efficiency at higher energies requires the condition[17]

$$R_{Cr} \geq \frac{2d}{\theta_{Cr}^2(E)} \quad\text{..}\quad (8)$$

to be satisfied. Here R_{Cr} is the radius of curvature of the fiber, d is the channel diameter and θ_{Cr} is the critical angle for total reflection. For borosilicate glass, the critical angle is given in milliradians by $\theta_{Cr} = 32 / E$ (keV). What equation (8) physically demands is small channel diameters and an absence of sharp bends, in order to transport high energy photons efficiently. Results of simulations with the new code for these optics have been fed back into manufacturing designs.

The defect analysis was a deviation from the research plan recorded in the original proposal. The thrust of this effort was to gain a scientific understanding of the factors that need to be controlled to engineer and design high quality optics.

5.4 Post-Defect Study Optics

More recent tapered prototypes, however have been free from these glass inclusions. Table 2 lists the dimensions of these optics. Transmission vs Energy for seven prototypes, each 17 cm in length with a input focal distance of 30 mm was measured and is plotted in figure 32.

Table 2: Dimensions of seven prototypes fabricated after the defect analysis.

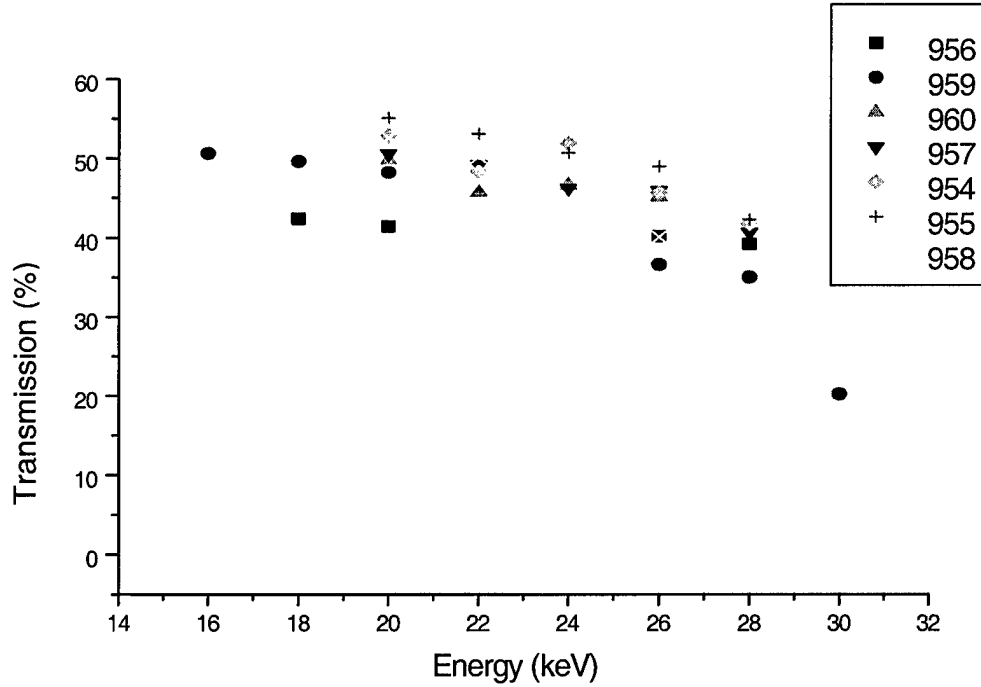|	Optic #	L,mm	ODin,mm (c-c)	ODout,mm (c-c)	F_{in},mm
1	954	170	2.9	4.33	300
2	955	170	2.86	4.36	300
3	956	170	2.88	4.35	300
4	957	170	2.87	4.35	300
5	958	170	2.85	4.34	300
6	959	170	2.89	4.36	300
7	960	170	2.85	4.35	300

Figure 32: Transmission vs energy results for the linear tapered prototypes listed in table 2. Transmisssion values close to 50% make these optics well suited for contrast and scatter transmission measurements in progress.

The data and knowledge obtained as a result of the detailed defect study carried out on the linear tapered optics have guided the fabrication process for subsequent manufacture of such optical components. The higher transmission prototypes listed in table 6 provide excellent material to carry out contrast and primary / scattered transmission measurements when these optics are employed in post-patient mode.

Section 6: Straight Bundle for Scatter Rejection

Because of the technological hurdles in manufacturing the curved monolithic optics, the fastest route to a large scale anti-scatter system for contrast measurements is a straight optic. The low angular acceptance of the capillary channels requires that the optic be used with a collimated beam as shown in figure 32.
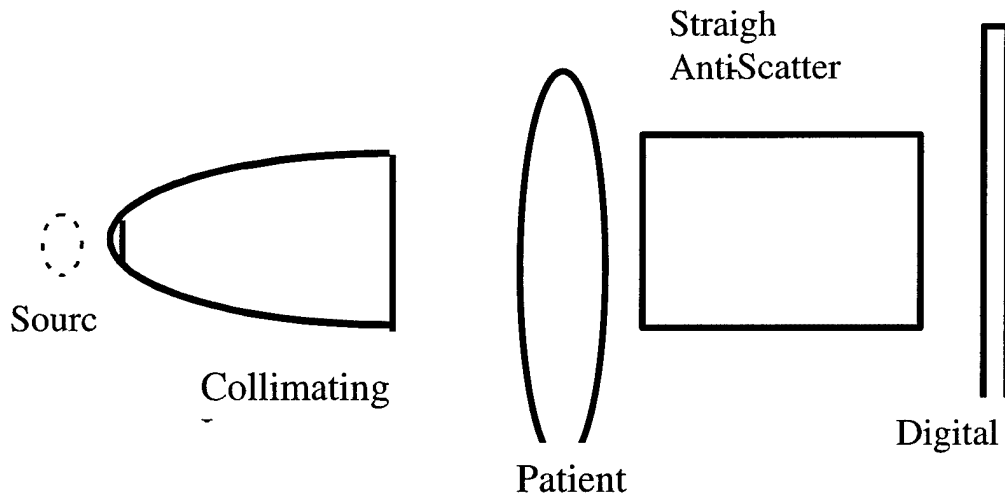

Figure 32 : Geometry for straight anti-scatter lens

Moreover, rather than simply using long air gaps to eliminate scatter, a straight polycapillary antiscatter optic could be employed. Such an antiscatter optic, essentially a 3 cm bundle of straight polycapillary fibers, was aligned to the

output of the collimating prototype I. The anti-scatter optic was 150 mm in length with 55 μm channels as seen in figure 33. The transmission spectrum of this optic is shown in figure 34.
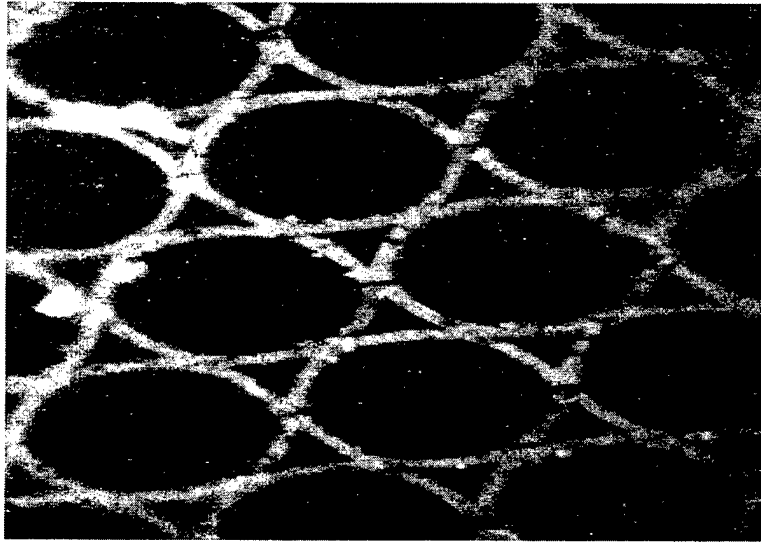

Figure 33: Straight lens fiber structure obtained, using an optical microscope.
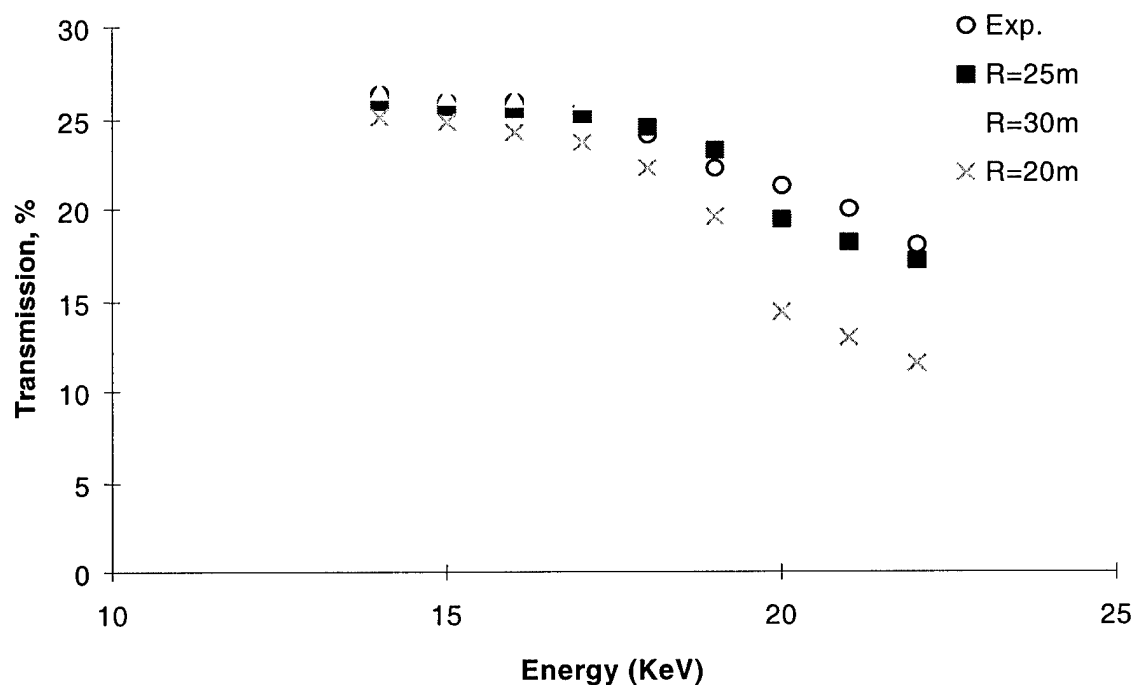
Figure 34: Transmission of straight anti-scatter lens compared to simulations. Simulation uses 1 nm roughness, 0.45 mrad waviness and 26% overall open area.

Simulations show that the apparently straight fibers seen in figure 34, have significant curvature, with a radius of curvature of about 25 m, and the optic has lower transmission than is acceptable for a post-patient optic.
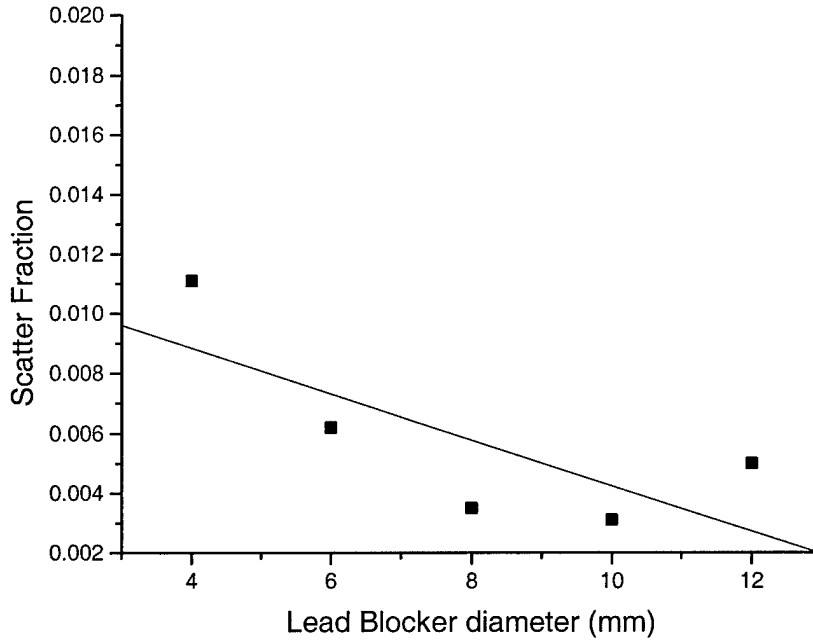
Section 7: Scatter Fraction Measurements

Fig 35: Scatter fraction measurement using the central straight fibers in prototype collimating optic II. These fibers are highly uniform in their performance.

An indicator of the potential of x-ray capillary optics as efficient scatter rejection devices for imaging purposes is demonstrated by the scatter fraction measurements shown in fig 35. The central core of the prototype collimating optic II, which comprises of straight fibers that transmit well and uniformly, was used for this measurement.

A lucite phantom was used before the optic and lead blocks of different dimensions were used to block parts of this phantom. The beam intensity right behind the lead blocker gives I_s, the scattered beam intensity. The beam intensity besides the blocker gives $I_s + I_p$, where I_p is the primary intensity.

Scatter fraction is then defined as $\dfrac{I_s}{I_s + I_p}$. The above measurement indicates a scatter fraction of close to 1%. Measurements are ongoing to compare this result, for the no optic case and with an air gap.

Section 8: Key Research Accomplishments and Reportable Outcomes

Polycapillary optics, composed of thousands on glass fibers strung together (multi-fiber optics) or pulled together into a single element (monolithic optics) have stimulated great interest in the x-ray community to explore their applications. These optics function to collimate, focus, filter x-rays and magnify / demagnify x-ray images to couple them to direct digital x-ray detectors.

Three multi-fiber collimating prototypes and a monolithic optic were characterized for potential application in digital mammography. Multi-fiber optics with their large dimensions are compatible with large emission area x-ray sources and are particularly suited for applications requiring wide x-ray fields. Multi-fiber I was essentially designed for 8 keV diffraction experiments. Multi-fiber II with a larger focal distance was designed with a larger radius of curvature for the fibers at the periphery of the holding structure. Multi-fiber III, specifically designed for potential applications in mammography demonstrated high transmission efficiency (~ 40 keV at 20 keV) and a uniformity of 10% rms across the optic cross-section. Experiments and analysis carried out at 20 keV, yielded detailed information on the alignment accuracies within the holding structure for the multi-fiber prototypes. These multifiber lenses can be subject to fiber misalignment on input, which can affect transmission performance. The exit angle divergence analysis showed that the output end of multi-fiber I was slightly convergent rather than parallel. Bending and waviness, which change the angle of incidence at every bounce, have a deleterious effect on the optic transmission. Channel waviness can also increase the beam divergence significantly compared to an ideal lens.

Bulk multi-fiber collimating optics can be manufactured with good design compliance. However, using a collimating device alone in an imaging unit as a pre-patient device is not a viable option due to the exit beam divergence. For a 5 cm thick patient, the geometrical blur would be 85 microns, giving a resolution of 6 lp / mm. This resolution is insufficient for mammography, so the lens cannot be

used without some means, such as a diffracting crystal, being applied to reduce the divergence. Polycapillary collimating optics can offer diffracted beam intensity gains of two orders of magnitude higher than that available from systems employing pinholes or slits. A 50 kW source employed in conjunction with polycapillary optics and high mosaicity crystals can provide the photon flux required for monochromatic imaging.

Monochromatic imaging can provide enhanced contrast and resolution in conjunction with the elimination of scatter and reduced dose. Image contrast is also enhanced by the elimination of scattered radiation by a large air gap made available by the extremely parallel beam. Resolution is enhanced by the concomitant elimination of geometric blur. Finally dose reduction takes place due to the absence of low energy photons that are absorbed in the patient. The reflected beam count rate for a crystal used with a polycapillary collimator (T =

with an angular band-width of 0.5 mrad is about $3.1 * 10^{9} \dfrac{\text{photons}}{\text{cm}^{2}\ \text{sec}}$, which may be

high enough for monochromatic imaging.

Optics characterized for post-patient scatter rejection devices included straight fiber bundles and tapered monolithics designed for magnification. Scatter fraction measurements prove an excellent capability to eliminate Compton scattered photons from the image plane. Scatter fraction measurements on a lucite phantom yielded values of ~ 1%.

These optics are difficult to manufacture. To enhance the manufacturing yield, a systematic defect analysis including x-ray transmission as a function of optic length and photon energy, and optical microscopy, was performed. The primary defects consisted of localized glass inclusions. Recently manufactured optics have overcome this blockage problem. Defect-free optics have demonstrated transmissions of 50% at 20 keV.

Polycapillary optics can be effectively employed as pre-patient optics to generate wide area parallel monochromatic x-ray beams. Post-patient optics can be

utilized as scatter rejection optical elements. These optics coupled to direct digital x-ray detectors present tremendous potential to form an integrated digital mammography system, with high dynamic range, enhanced contrast and minimal patient dose.

Future work

Measurements are ongoing and shall continue on recently manufactured linear prototypes. Contrast detail phantoms used with the optic will provide contrast and scatter fraction information quantitatively. Prototype monolithic optics that have demonstrated superior performance in the measurements reported, have been put together to form a larger optic. Measurements will be carried out on this optic.

Monochromatic imaging holds a lot of promise in connection to increased resolution, enhanced contrast and reduced dose to the patient. The feasibility analysis presented here shall be complemented with detailed experimental work with multi-fiber collimating prototype III.

Bibliography

[1] Bruce H.Hasegawa, The Physics of Medical Imaging (Medical physics publishing company, Nov 1991.

[2] David Kruger et al, "Imaging characteristics of x-ray capillary optics in digital mammography", Medical Physics. 23, 187-196 (1996).

[3] Physics Today, November 1997.

[4] Wei Zhao and John A. Rowlands, " A large area solid state detector for radiology using amorphous selenium", SPIE vol. 1651 Medical imaging ∨I: Instrumentation (1992)

[5] H.H. Rossi and A M. Kellerer, "Roentgen", Radiation research, 144, 124-128 (1995)

[6] C.A. MacDonald et al, " Quantitative measurements of the performance of Capillary x-ray optics", in Multilayer and Grazing incidence x-ray/EUV optics II, edited R.B. Hoover and A.Walker, SPIE Proc. Vol. 2011, (1993)

[7] J.B. Ullrich, V.Kovantsev and C.A. MacDonald, " Measurements of Polycapillary x-ray optics," J.Appl. Phys. 74 (10), 5933-5939 (1993)

[8] A.H. Compton and S.K. Allison, " X-rays in theory and experiment " D. Van Nostrand company, Inc, New York.

[9] Studies of Monolithic Capillary optics for small sample crystallography " Johannes ullrich, A Ph.D dissertation, Department of Physics, state University Of New York At Albany.

[10] " Studies of Monolithic Capillary optics for small sample crystallography " Johannes ullrich, A Ph.D dissertation, Department of Physics, state University Of New York At Albany.

[11] F. Arfelli, A.Bravin, G.Barbielinni et al, "Digital mammography with synchrotron radiation" Rev.Sci.Instr., Vol 66, No.2, Febraury 1995.

[12] J.M. Boone and J. A Seibert, Med. Phys. 21 (1994) 1853

[13] R.J.Jennings, P.W.Quinn et al, SPIE Proc. 1896 (1993) 259.

[14] A.K.Freund, Nuclear.Instr.Meth.A 266 (1988) 461

[15] Q.F.Xiao, J.C.Kimball et al, " Numerical Simulations for Capillary-based X-ray optics" in X-ray detector physics and applications, R.B.Hoover ed, SPIE vol.1736,pp227-238,1992

[16] Lei Wang, B.K.Rath, W.M.Gibson, J.C.Kimball, C.A.MacDonald, "Performance study of Polycapillary optic performance for hard x-rays", Journal of Applied Physics, 80 (7),pp.3628-3638, October 1, 1996.

[17] C.A.MacDonald "Applications and Measurements of Polycapillary X-ray optics", Journal of X-ray science and Technology 6, 32-47 (1996)